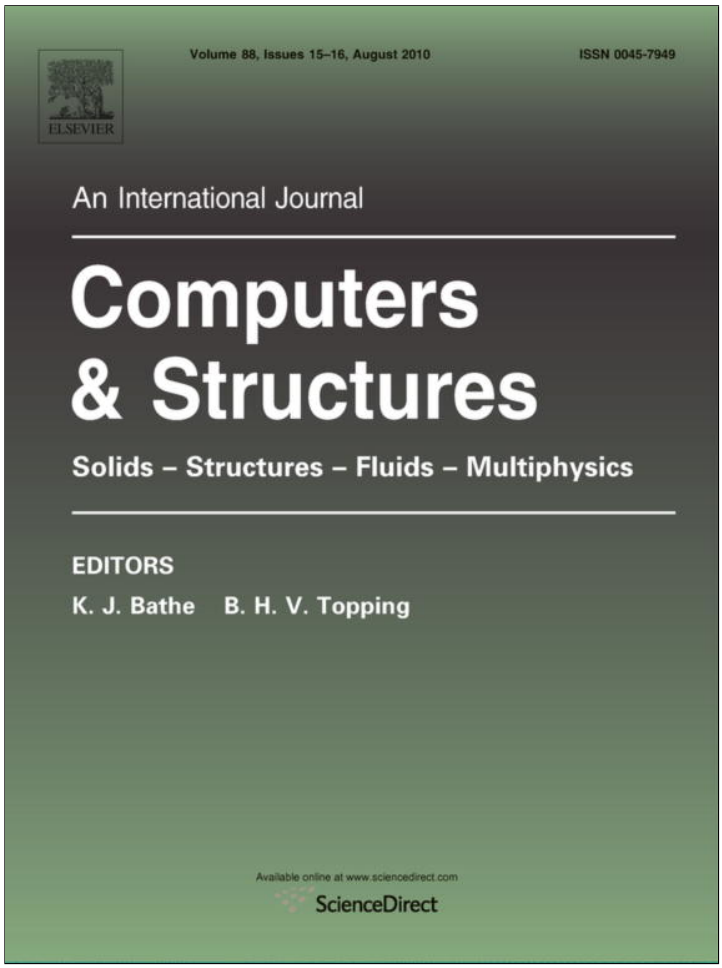

Computers and Structures 88 (2010) 909–923

Contents lists available at ScienceDirect

Computers and Structures

journal homepage: www.elsevier.com/locate/compstruc

Meshfree simulations of plugging failures in high-speed impacts

Bo Ren [a,b], Shaofan Li [a,c,*]

[a] Department of Civil and Environmental Engineering, University of California, Berkeley, CA 94720, USA
[b] School of Hydro-Power and Information Engineering, Huazhong University of Science and Technology, Wuhan, China
[c] School of Civil Engineering and Mechanics, Huazhong University of Science and Technology, Wuhan, China

ARTICLE INFO

Article history:
Received 3 August 2009
Accepted 5 May 2010
Available online 9 June 2010

Keywords:
Contact
Impact
Ductile fracture
Meshfree method
Plugging fracture

ABSTRACT

A meshfree method and (the related) a specified crack growth algorithm are used to simulate plugging fracture during high-speed impacts. In particular, we are simulating ballistic penetration of a steel plate, which is a ductile failure process involving projectile and target collision, contact, and subsequent projectile penetration companied plugging fracture inside steel plate. We have developed and implemented an explicit meshfree Galerkin formulation, which is capable of capturing ductile fractures during finite inelastic deformation. The developed meshfree computational procedure has the following features: (1) it has an effective dynamic meshfree contact algorithm that is suitable for high-speed impact; (2) it can deal with thermal–mechanical couplings, and the stability of coupled thermal–mechanical motion is guaranteed by an adiabatic split algorithm that integrates adiabatic heating and heat diffusion separately; (3) it has an automatic crack growth algorithm that can simulate the whole lifespan of crack growth including crack nucleation, propagation and arrest; (4) to compute the rate-dependent material responses, a modified forward Euler tangent algorithm is adopted in constitutive update process for the nonlinear thermal–mechanical inelastic constitutive relation that takes into account damage evolution. Results of a numerical simulation of plugging fracture due to projectile/target impact are presented, and they compare well with experimental data.

1. Introduction

Ductile material failures during high-speed impact and penetration have been a main concern in designing armored vehicles, sea vessels, and their reliability analysis. Most high-speed impact/contact problems are involved finite deformation and subsequently material and structural damages induced by high strain rates and shock waves. To accurately predict such physical process and to precisely quantify the thermal–mechanical field variables are the key for novel material and structure designs.

In recent years, there have been some studies on numerical simulations of high-speed impact and contact problems in the literatures, such as simulations of vehicle crashworthiness, e.g. [5,17,1], and ballistic impact and penetration, e.g. [12,9–11,35,24]. However, most of these simulations have remained in the stage of academic research. To capture the dramatic changes and evolution in structure geometry and material constitutive relations during high-speed impacts and to accurately predict ductile failure process have remained to be challenges of computational failure mechanics.

During impact and penetration process, a ductile solid will be undergoing severe local deformation with extremely high strain rates and high temperature, which lead to material damage and fracture. These pose serious challenges for computational study, for instance, how to simulate crack growth in ductile materials. Although there are some techniques developed in finite element methods such as the automatic remesh technology by Wawrzynek and Ingraffea [30], finite element based methods seem not to be very successful in ductile fracture simulations. This is because the ductile fracture is a thermodynamically irreversible process, which prohibits artificial numerical unloading. On the other hand, meshfree interpolations have flexibility to adapt computational domain with evolving topological structure without numerical unloading. Recently, there have been quite a few research works using meshfree methods to simulate crack growth, e.g. [6,7,14,26] among others. In particular, Li and his co-workers have developed a meshfree crack growth algorithm specifically suitable for ductile fracture [22,27,28]. In this work, we want to extend the meshfree failure algorithm to simulate plugging failure formed by crack propagation during high-speed impact and contact. To do so, we have to address a number of technical issues: (1) Physically, the plugging fracture induced by high-speed impact is initiated by two-body or multi-body contacts. Although, the impact/contact algorithm has been well developed in finite element method, there

* Corresponding author at: Department of Civil and Environmental Engineering, University of California, Berkeley, CA 94720, USA. Tel.: +1 510 642 5362; fax: +1 510 643 8928.
E-mail address: shaofan@berkeley.edu (S. Li).

0045-7949/$ - see front matter © 2010 Elsevier Ltd. All rights reserved.
doi:10.1016/j.compstruc.2010.05.003

are still many pragmatic issues for the meshfree contact impact algorithm and its actual implementation. In this work, based on general philosophy of master/slave slide interface algorithm from finite element method, a master/slave contact algorithm is developed to fit to meshfree computations. (2) During high-speed impact, a large amount of heat will generated nearby the failure area by plastic work accompanied by heat conduction; the thermal–mechanical coupling will cause thermal softening and material instability, which manifests as micro void formation and coalescence, subsequent macro material damage and fracture. To model such complex constitutive behaviors, we adopt the Johnson–Cook model in constitutive modeling, and use a modified forward Euler one step time integration in constitutive update based on a tangent modulus method by Peirce et al. [25]. Although the Johnson–Cook model is a thermal-related model, the heat conduction process is considered by many researchers. In this work, fully coupled thermal–mechanical equations of motion are considered with heat conduction, large scale yielding, and finite deformation. To ensure the numerical stability, an operator splitting algorithm is adopted to update thermal–mechanical constitutive and to integrate the weak form of heat conduction equation.

The paper is organized into six sections: in Section 2, we shall present a complete meshfree Galerkin weak formulation, its interpolation and constitutive update; in Section 3, we shall discuss the meshfree impact/contact algorithm, and in Section 4, we shall outline a meshfree crack growth algorithm. The results of the plugging fracture simulation are presented in Section 5, and a few remarks are made in Section 6.

2. Meshfree Galerkin formulation with the Johnson–Cook model

2.1. Basic formulas

To fix notation, we firstly describe basic kinematic definitions that will be lately used in the constitutive update. Initially at $t = t_0$, the meshfree particle position in the reference configuration is denoted by $\mathbf{X}$. In the current configuration at time $t = t_n$, the position of the same meshfree particle is denoted by $\mathbf{x} = \boldsymbol{\phi}(\mathbf{X})$, where $\boldsymbol{\phi}$ is the deformation map. The deformation gradient is then defined as:

$$\mathbf{F} = \frac{\partial \mathbf{x}}{\partial \mathbf{X}} = x_{i,J}\mathbf{e}_i \otimes \mathbf{E}_J \tag{2.1}$$

where $\mathbf{e}_i$ denote the coordinate basis vectors in the current configuration, and $\mathbf{E}_J$ denote the coordinate basis vectors in the reference configuration. The velocity gradient in the current configuration is,

$$\ell = \frac{\partial \mathbf{v}}{\partial \mathbf{x}} \tag{2.2}$$

It can be split into two parts, a symmetric part and an anti-symmetric part as the rate of deformation and the rate of spin:

$$\ell = \boldsymbol{d} + \mathbf{w} \tag{2.3}$$

$$\boldsymbol{d} = (\ell + \ell^T)/2 \tag{2.4}$$

$$\boldsymbol{w} = (\ell - \ell^T)/2 \tag{2.5}$$

In this paper, a total Lagrangian approach is adopted to represent the finite deformation of solid. Therefore, ℓ should be expressed in term of the deformation gradient:

$$\ell = \dot{\mathbf{F}} \cdot \mathbf{F}^{-1} \tag{2.6}$$

where $\dot{\mathbf{F}} = \frac{\partial \mathbf{v}}{\partial \mathbf{X}}$.

Finally, the rate of deformation and the spin tensors can be expressed in terms of deformation gradient in reference configuration:

$$\boldsymbol{d} = (\dot{\mathbf{F}} \cdot \mathbf{F}^{-1} + \mathbf{F}^{-T} \cdot \dot{\mathbf{F}}^T)/2 \tag{2.7}$$

$$\boldsymbol{w} = (\dot{\mathbf{F}} \cdot \mathbf{F}^{-1} - \mathbf{F}^{-T} \cdot \dot{\mathbf{F}}^T)/2 \tag{2.8}$$

The Jaumann rate of Kirchhoff stress is defined as:

$$\overset{\triangledown}{\boldsymbol{\tau}} = \dot{\boldsymbol{\tau}} - \boldsymbol{w} \cdot \boldsymbol{\tau} + \boldsymbol{\tau} \cdot \boldsymbol{w} \tag{2.9}$$

Define a deviatoric stress tensor $\mathbf{s}$ as:

$$\mathbf{s} = \boldsymbol{\tau} - \frac{1}{3}(\boldsymbol{\tau} : \mathbb{I})\mathbb{I} \tag{2.10}$$

where $\mathbb{I}$ is the second order unit tensor.

The von Mises effective stress can be defined as:

$$\bar{\tau} = \sqrt{\frac{3}{2}\mathbf{s} : \mathbf{s}} \tag{2.11}$$

The accumulated effective plastic strain is

$$\bar{\varepsilon} = \int_0^t \dot{\bar{\varepsilon}}\, dt \tag{2.12}$$

where $\dot{\bar{\varepsilon}}$ is the rate of effective plastic strain.

2.2. Thermal–mechanical coupling

The high-speed impact process will produce enormous plastic deformation, and in turn the material plastic flow will generate a large amount of heat at some local area. In some spatial points, the temperature can sharply increase up close to melting temperature. For instance, this may happen at the tip of Adiabatic Shear Band in less than 200 μs [36,37]. Therefore the effects of thermal–mechanical coupling and heat conduction cannot be neglected in high-speed impact simulations. In this work, a fully coupled thermal–mechanical impact problem with inelastic damage evolution is considered.

By the virtual power principle, the weak formulation of balance of the linear momentum can be written as:

$$\int_{\Omega_0} \mathbf{P} : \delta\mathbf{F}\, d\Omega = \int_{\Gamma_0^T} \mathbf{T} \cdot \delta\mathbf{u}\, dS - \int_{\Omega_0} \rho_0 \frac{\partial^2 \mathbf{u}}{\partial t^2} \cdot \delta\mathbf{u}\, d\Omega \tag{2.13}$$

where $\mathbf{P}$ denotes the nominal stress, which is the transpose of the first Piola–Kirchhoff stress, and it can be related to the Kirchhoff stress as $\boldsymbol{\tau} = \mathbf{P}\mathbf{F}^T$; and Γ_0^T denotes the traction boundary where the traction force $\mathbf{T}$ is prescribed. The above weak form formulation is obtained by integration by parts of the balance equation of linear momentums.

Considering the heat generation and conduction process, the strong form of energy equation can be written as:

$$\rho_0 C_p \frac{\partial T}{\partial t} = \chi \boldsymbol{\tau} : \mathbf{d}^p + \nabla_X (J\mathbf{F}^{-1} \cdot \mathbf{K} \cdot \mathbf{F}^{-T} \cdot \nabla_X T) \quad \forall \mathbf{X} \in \Omega_0 \tag{2.14}$$

where T is the temperature, χ denotes the fraction of plastic work converting to heat, ∇_X is the gradient operator in reference configuration, C_p is specific heat. For isotropic heat conduction, the heat conductivity tensor $\mathbf{K} = \kappa\mathbb{I}$, where κ is the conductivity coefficient. $\mathbf{d}^p$ is the plastic rate of deformation.

In general, the simulation of such coupled thermo-mechanical problem is a complex and difficult process. An effective integration scheme to solve such coupled thermal–mechanical equations is so-called operator splitting method, which is proposed by Armero and Simo [2]. In their scheme, a fractional time step method is adopted that is associated with an operator split of a fully nonlinear thermal–mechanical system into an adiabatic heat generation phase, followed by a heat conduction phase at the fixed configuration. Following the same procedure, the strong form energy balance equation may be also divided into the heat generation part and the heat conduction part:

$$\rho_0 C_p \frac{\partial T}{\partial t} = \chi \boldsymbol{\tau} : \mathbf{d}^p \tag{2.15}$$

and

$$\rho_0 C_p \frac{\partial T}{\partial t} = \nabla_X (J\mathbf{F}^{-1} \cdot \mathbf{K} \cdot \mathbf{F}^{-T} \cdot \nabla_X T) \tag{2.16}$$

For adiabatic heating, the least square weighted residual equation is:

$$\int_{\Omega_0} \rho_0 C_p \frac{\partial T}{\partial t} \delta T \, d\Omega = \int_{\Omega_0} \chi \boldsymbol{\tau} : \mathbf{d}^p \delta T \, d\Omega \tag{2.17}$$

In this work, the material modeling is accomplished by adopting a thermal–mechanical coupled Johnson–Cook model. For this model, we can show that:

$$\chi \boldsymbol{\tau} : \mathbf{d}^p \approx \chi \bar{\tau} \cdot \dot{\bar{\varepsilon}} \quad \forall \mathbf{x} \in \Omega(t) \tag{2.18}$$

The weak form of heat conduction equation is:

$$\int_{\Omega_0} \rho_0 C_p \frac{\partial T}{\partial t} \delta T \, d\Omega = \int_{\partial\Omega_0} J(\mathbf{F}^{-1} \cdot \mathbf{K} \cdot \mathbf{F}^{-T} \nabla_X T) \cdot \mathbf{N} \delta T \, dS - \int_{\Omega_0} J(\mathbf{F}^{-1} \cdot \mathbf{K} \cdot \mathbf{F}^{-T} \nabla_X T) \nabla_X (\delta T) d\Omega \tag{2.19}$$

The first term of the left-hand side of above equation is the boundary heat dissipation. Because the response time for high-speed impact/penetration only last for a few milliseconds; and normally the heat generated inside solid does not have enough time to dissipate into the ambient environment. For simplicity, we may ignore the part of heat that dissipates into the surrounding environment. Hence, the weak form of heat conduction equation becomes:

$$\int_{\Omega_0} \rho_0 C_p \frac{\partial T}{\partial t} \delta T \, d\Omega = -\int_{\Omega_0} (J\mathbf{F}^{-1} \cdot \mathbf{K} \cdot \mathbf{F}^{-T} \nabla_X T) \nabla_X (\delta T) d\Omega \tag{2.20}$$

Finally, the energy balance equation including heat generation and conduction becomes

$$\int_{\Omega_0} \rho_0 C_p \frac{\partial T}{\partial t} \delta T \, d\Omega = \int_{\Omega_0} \chi \bar{\tau} \dot{\bar{\varepsilon}} \delta T \, d\Omega - \int_{\Omega_0} (J\mathbf{F}^{-1}\mathbf{K} \cdot \mathbf{F}^{-T} \nabla_X T) \nabla_X (\delta T) d\Omega \tag{2.21}$$

2.3. Thermal–mechanical meshfree formuluation

The weak forms of balance of linear momentum, heat generation, and heat conduction are expressed in Eqs. (2.13) and (2.21). The corresponding boundary conditions in referential configuration are,

$$\mathbf{P} \cdot \mathbf{N} = \boldsymbol{T}^0 \quad \forall \mathbf{X} \in \Gamma_t \tag{2.22}$$

$$\mathbf{u} = \bar{\mathbf{u}} \quad \forall \mathbf{X} \in \Gamma_u \tag{2.23}$$

Here, Γ_t and Γ_u denote the traction boundary and essential boundary, and $\mathbf{N}$ is the unit normal vector of Γ_t.

It should be noted that the meshfree interpolation used here is not able to represent boundary data via boundary value interpolation. Therefore, an extra term appears in the weak form Eq. (2.13)

$$\int_{\Gamma_u} \boldsymbol{T}^0 \cdot \delta \mathbf{u} \, d\Gamma_X \tag{2.24}$$

because $\delta \mathbf{u} \neq \mathbf{0} \ \forall \mathbf{X} \in \Gamma_u$. On how to estimate this term and enforce the essential condition for meshfree methods, the readers is referred to Li and Liu [18].

By meshfree discretization, the temperature field may be interpolated by a temperature array of all particles:

$$\mathcal{T}(t) = \{T_1, T_2, \ldots, T_{np}\}^T \tag{2.25}$$

The displacement and temperature fields can be approximated by the meshfree interpolation,

$$\mathbf{u}^h(\mathbf{X}, t) = \sum_{I=1}^{np} N_I(\mathbf{X}) \mathbf{U}_I(t) \quad \text{with } \mathbf{U}_I(t) = \{U_{I1}, U_{I2}, U_{I3}\}^T \tag{2.26}$$

$$\delta \mathbf{u}^h(\mathbf{X}, t) = \sum_{I=1}^{np} N_I(\mathbf{X}) \delta \mathbf{U}_I(t) \tag{2.27}$$

$$T^h(\mathbf{X}, t) = \sum_{I=1}^{np} N_I(\mathbf{X}) T_I(t) \tag{2.28}$$

$$\delta T^h(\mathbf{X}, t) = \sum_{I=1}^{np} N_I(\mathbf{X}) \delta T_I(t) \tag{2.29}$$

The weak form Eq. (2.13) will then lead to a set of discrete dynamicsal equations:

$$\mathbf{M} \frac{d^2 \mathbf{u}}{dt^2} = \mathbf{f}^{ext} - \mathbf{f}^{int} \tag{2.30}$$

The conventional row-sum lumped mass matrix $\mathbf{M}$ is adopted for explicit time integration scheme, and the external and internal force arrays are calculated as follows:

$$\mathbf{f}_I^{ext} = \int_{\Gamma_T} T_i(X, t) N_I \mathbf{E}_i \, dS \tag{2.31}$$

$$\mathbf{f}_I^{int} = \int_{\Gamma_x} P_{ij}^h \frac{\partial N_I}{\partial X_J} \mathbf{E}_i \, d\Omega \tag{2.32}$$

where $\mathbf{E}_i$ is the unit vector of referential coordinate.

Then the energy balance equation (2.21) becomes

$$\mathbf{C}_p \cdot \dot{\mathcal{T}} = \mathbf{G} - \mathbf{H} \cdot \mathcal{T} \tag{2.33}$$

where $\mathbf{C}_p$ is defined as the specific thermal mass, $\mathbf{G}$ is the matrix related to heat generation due to plastic strain, $\mathbf{H}$ is the matrix related to heat conductivity:

$$\mathbf{C}_p = [C_{pIJ}], \quad C_{pIJ} := \int_{\Omega_X} \rho_0 C_p N_I(\mathbf{X}) N_J(\mathbf{X}) d\Omega_X \tag{2.34}$$

$$\mathbf{G} = [G_{IJ}], \quad G_{IJ} := \int_{\Omega_X} \chi \bar{\tau} \dot{\bar{\varepsilon}} N_I(\mathbf{X}) N_J(\mathbf{X}) d\Omega_X \tag{2.35}$$

$$\mathbf{H} = [H_{ij}], \quad H_{ij} := \int_{\Omega_X} \kappa F_{I\ell}^{-1}(\mathbf{X}) F_{\ell J}^{-T}(\mathbf{X}) N_{i,J}(\mathbf{X}) N_{j,I}(\mathbf{X}) d\Omega_X \tag{2.36}$$

where Ω_X is the integration weight for each particle in the background grid.

In this paper, the shape function of the Reproducing Kernel Particle Method (RKPM) is chosen as the meshfree interpolation function $N_I(\mathbf{X})$ (see [23]). The RKPM shape function may be viewed as an enhanced version of the original SPH shape function. The basic ideal of RKPM is to construct a proper kernel function by 'correcting' the original SPH kernel function, $w(\mathbf{X} - \overline{\mathbf{X}})$, to satisfy the partition of unity condition so that the rigid body motion and linear deformation can be correctly represented. The RKPM interpolation function can be represented as:

$$\mathbf{u}^h(\mathbf{X}, t) = \int_{\Omega} \mathbf{C}(\mathbf{X}, \overline{\mathbf{X}}) w(\mathbf{X} - \overline{\mathbf{X}}) \mathbf{u}(\overline{\mathbf{X}}) d\Omega_{\overline{\mathbf{X}}} \tag{2.37}$$

Here, the original kernel function $w(\mathbf{X} - \overline{\mathbf{X}})$ is obtained by a Cartesian product of the one-dimensional cubic spline function (see [23]), and $\mathbf{C}(\mathbf{X}, \overline{\mathbf{X}})$ is called the Correction function:

$$\mathbf{C}(\mathbf{X}, \overline{\mathbf{X}}) = \mathbf{b}^T(\mathbf{X}) \mathbf{p}(\mathbf{X}, \overline{\mathbf{X}}) \tag{2.38}$$

In above formulation, $\mathbf{p}(\mathbf{X}, \overline{\mathbf{X}})$ could be any suitable basis function. In this paper, we choose the first order polynomials or bi-linear polynomials as the basis function:

$$\mathbf{p}^T(\mathbf{X},\overline{\mathbf{X}}) = [1, x-\bar{x}, y-\bar{y}, (x-\bar{x})(y-\bar{y})] \tag{2.39}$$

and $\mathbf{b}(\mathbf{X})$ is a coefficient vector, it is determined by the reproducing condition [23], which will leads to the following vector equation:

$$\mathbf{b}(\mathbf{X}) = \mathbf{M}^{-1}(\mathbf{X})\mathbf{p}(0) \tag{2.40}$$

where

$$\mathbf{M}(\mathbf{X}) = \int_{\Omega} \mathbf{p}(\mathbf{X}-\overline{\mathbf{X}})\mathbf{P}^T(\mathbf{X}-\overline{\mathbf{X}})w(\mathbf{X}-\overline{\mathbf{X}})d\Omega_{\overline{\mathbf{X}}} \tag{2.41}$$

$$\mathbf{p}^T(0) = [1,0,0,0] \tag{2.42}$$

Assume that in the domain Ω there is a valid particle distribution by np particles. The RKPM kernel function is compact supported, finally, the kernel integration, Eq. (2.37), can be discretized to form a numerical interpolation:

$$\mathbf{u}^h(\mathbf{X},t) = \sum_{I=1}^{np} \mathbf{C}(\mathbf{X},\overline{\mathbf{X}})w(\mathbf{X}-\overline{\mathbf{X}})\mathbf{U}_I(t)\Delta V_I \tag{2.43}$$

$$= \sum_{I=1}^{np} N_I(\mathbf{X})\mathbf{U}_I(t) \tag{2.44}$$

where ΔV_I is integration weight and finally, the RKPM interpolation function is then defined as:

$$N_I(\mathbf{X}) = \mathbf{C}(\mathbf{X},\overline{\mathbf{X}})w(\mathbf{X}-\overline{\mathbf{X}})\Delta V_I \tag{2.45}$$

2.4. Constitutive model

During high-speed impact, the propagation of shock wave induces high strain rate plastic deformation, and most of the plastic work will convert to heat [29], and consequently it leads to material softening. Hence, the mechanical response of material is a rate-dependent thermal–mechanical phenomenon. In this paper, a tangent model proposed by Peirce et al. [25] is adopted to update the constitutive relation. This method is used by Li et al. [22] firstly, in this paper, we re-derived the formula and correct some errors in the paper by Simkins and Li [28].

For ductile fracture problem, the total deformation may be decomposed to three parts: elastic, plastic, and thermal part:

$$\mathbf{d} = \mathbf{d}^e + \mathbf{d}^p + \mathbf{d}^T \tag{2.46}$$

A rate form constitutive equation is used:

$$\overset{\nabla}{\boldsymbol{\tau}} = \mathbf{C} : \mathbf{d}^e = \mathbf{C} : (\mathbf{d} - \mathbf{d}^p - \mathbf{d}^T) \tag{2.47}$$

In case of isotropic hardening:

$$\mathbf{d}^p = \dot{\bar{\varepsilon}}\hat{\mathbf{n}} \tag{2.48}$$

where $\hat{\mathbf{n}}$ is the normal of deviatoric stress:

$$\hat{\mathbf{n}} = \frac{3}{2\bar{\tau}}\mathbf{s} \tag{2.49}$$

In adiabatic heating, the rate of deformation induced by thermal effect is

$$\mathbf{d}^T = \alpha\dot{T}\mathbb{I} \tag{2.50}$$

where α is the coefficient of thermal expansion, and $\mathbb{I}$ is the second order unit tensor.

Based on the Johnson–Cook model [15,16] the plastic strain rate $\dot{\bar{\varepsilon}}$ is calculated as follows:

$$\dot{\bar{\epsilon}} = \dot{\epsilon}_0 \exp\left\{\frac{1}{C}\left(\frac{\tau_Y}{g(\bar{\epsilon},T)} - 1\right)\right\} \tag{2.51}$$

$$g(\bar{\epsilon},T) = [A + B\bar{\epsilon}^n][1-\mathcal{T}^m] \quad \text{with } \mathcal{T} = \frac{T-T_0}{T_m-T_0} \tag{2.52}$$

where $\dot{\epsilon}_0$ is a referential strain rate, normally, we choose it as 1.0 s^{-1}, n and m are strain hardening and thermal softening parameters, T_0 is the room temperature, and T_m is the melting temperature.

In usual explicit time integration, the basic field variables such as stresses, strains are calculated explicitly based on the information of the previous time step as computation progresses. To enhance the accuracy of the time integration, we adopt a fractional time increment scheme that evaluates the time derivatives of field variables at a time instance $t_{n+\theta}$ that is between t_n and T_{n+1}. To illustrate the procedure, we discuss how to update the Kirchhoff stress τ from $t = t_n$ to $t = t_{n+1}$,

$$\boldsymbol{\tau}_{n+1} = \boldsymbol{\tau}_n + \dot{\boldsymbol{\tau}}_\theta \Delta t \tag{2.53}$$

where $\dot{\boldsymbol{\tau}}_\theta$ is the Kirchhoff stress at predicted step t_θ, $\theta \in [0,1]$. From Eq. (2.9), we obtain,

$$\dot{\boldsymbol{\tau}}_\theta = \overset{\nabla}{\boldsymbol{\tau}}_\theta + \mathbf{w}_n \cdot \boldsymbol{\tau}_n - \boldsymbol{\tau}_n \cdot \mathbf{w}_n^T \tag{2.54}$$

From Eq. (2.47), $\overset{\nabla}{\boldsymbol{\tau}}_\theta$ can be written as:

$$\overset{\nabla}{\boldsymbol{\tau}}_\theta = \mathbf{C} : (\mathbf{d}_\theta - \dot{\bar{\epsilon}}_\theta \hat{\mathbf{n}}_\theta - \alpha\dot{T}_\theta \mathbb{I}) \tag{2.55}$$

To reduce the complexity of the computational algorithm, while computing the energy equation at a quadrature point, we first consider adiabatic heat generation:

$$\dot{T}_\theta = \frac{\chi}{\rho C_p}\bar{\tau}\dot{\bar{\varepsilon}}_\theta \tag{2.56}$$

Following the spirit of the tangent modulus method proposed by Peirce et al. [25], we consider,

$$\Delta\varepsilon = \Delta t\dot{\bar{\epsilon}}_\theta = \Delta t[(1-\theta)\dot{\bar{\epsilon}}_n + \theta\dot{\bar{\epsilon}}_{n+1}] \tag{2.57}$$

Here $\Delta\varepsilon$ can be approximated by Taylor expansion

$$\Delta\bar{\epsilon} = \dot{\bar{\epsilon}}_t\Delta t + \theta(\Delta t)^2\left[\left.\frac{\partial\dot{\bar{\epsilon}}}{\partial\bar{\epsilon}}\right|_t \dot{\bar{\epsilon}}_\theta + \left.\frac{\partial\dot{\bar{\epsilon}}}{\partial\tau_Y}\right|_t \dot{\bar{\tau}}_\theta + \left.\frac{\partial\dot{\bar{\epsilon}}}{\partial T}\right|_t \dot{T}_\theta\right] + \mathcal{O}(\Delta t^3) \tag{2.58}$$

hence

$$\dot{\bar{\epsilon}}_\theta = \dot{\bar{\epsilon}}_t + \theta(\Delta t)\left[\left.\frac{\partial\dot{\bar{\epsilon}}}{\partial\bar{\epsilon}}\right|_t \dot{\bar{\epsilon}}_\theta + \left.\frac{\partial\dot{\bar{\epsilon}}}{\partial\tau_Y}\right|_t + \left.\frac{\partial\dot{\bar{\epsilon}}}{\partial T}\right|_t \dot{T}_\theta\right] + \mathcal{O}(\Delta t^3) \tag{2.59}$$

where

$$\frac{\partial\dot{\bar{\epsilon}}}{\partial\bar{\epsilon}} = \dot{\bar{\epsilon}}\left\{-\frac{1}{C}\frac{\bar{\tau}}{g^2(\bar{\epsilon},T)}\right\}\left(\frac{\partial g}{\partial\bar{\epsilon}}\right) \tag{2.60}$$

$$\frac{\partial g}{\partial\bar{\epsilon}} = Bn\bar{\epsilon}^{(n-1)}(1-\mathcal{T}^m) \tag{2.61}$$

$$\frac{\partial\dot{\bar{\epsilon}}}{\partial\tau_Y} = \frac{\dot{\bar{\epsilon}}}{C g(\bar{\epsilon},T)} \tag{2.62}$$

$$\frac{\partial\dot{\bar{\epsilon}}}{\partial T} = \dot{\bar{\epsilon}}\left(-\frac{1}{C}\frac{\bar{\tau}}{g^2(\bar{\epsilon},T)}\right)\left(\frac{\partial g}{\partial T}\right) \tag{2.63}$$

$$\frac{\partial g}{\partial T} = -\frac{m\mathcal{T}^{m-1}}{(1-\mathcal{T}^m)(T_m-T_0)}g(\bar{\epsilon},T) \tag{2.64}$$

In finite deformation,

$$\dot{\bar{\tau}} = \hat{\mathbf{n}} : \overset{\nabla}{\boldsymbol{\tau}} \tag{2.65}$$

then we have,

$$\dot{\bar{\tau}}_\theta = \hat{\mathbf{n}}_\theta : \{\mathbf{C} : (\mathbf{d}_\theta - \mathbf{d}_\theta^p - \mathbf{d}_\theta^T)\} = \hat{\mathbf{n}}_\theta : \{\mathbf{C} : \mathbf{d}_\theta - \dot{\bar{\varepsilon}}_\theta\mathbf{C} : \hat{\mathbf{n}} - \frac{\alpha\chi}{\rho C_p}\bar{\tau}\dot{\bar{\varepsilon}}_\theta(\mathbf{C} : \mathbb{I})\} \tag{2.66}$$

Denoting

$$\mathbf{P}_\theta = \mathbf{C} : \hat{\mathbf{n}}_\theta \quad \text{and} \quad \mathbf{A}_\theta = \hat{\mathbf{n}} : \mathbf{C} : \hat{\mathbf{n}} \tag{2.67}$$

$\dot{\bar{\tau}}_\theta$ can be derived as,

$$\dot{\bar{\tau}}_\theta = \mathbf{P}_\theta : \mathbf{d}_\theta - \dot{\bar{\epsilon}}_\theta \mathbf{A}_\theta - \frac{3K\alpha\chi}{\rho C_p}\bar{\tau}_\theta \dot{\bar{\epsilon}}_\theta tr(\mathbf{P}_\theta) \tag{2.68}$$

By inserting Eqs. (2.56) and (2.68) to Eq. (2.59), we can obtain the following equation:

$$\dot{\bar{\epsilon}}_\theta = \frac{\dot{\bar{\epsilon}}_t}{1+\xi} + \frac{\xi}{(1+\xi)H_\theta}\mathbf{P}_\theta : \mathbf{d}_\theta \tag{2.69}$$

where

$$H_\theta = A_\theta + \frac{3K\alpha\chi}{\rho C_p}\bar{\tau}_\theta tr(\mathbf{P}_\theta) - \left(\frac{\partial\dot{\bar{\epsilon}}/\partial\bar{\epsilon}}{\partial\dot{\bar{\epsilon}}/\partial\bar{\tau}_\theta} + \frac{\chi\bar{\tau}_\theta}{\rho C_p}\left(\frac{\partial\dot{\bar{\epsilon}}/\partial T}{\partial\dot{\bar{\epsilon}}/\partial\bar{\tau}_\theta}\right)\right) \tag{2.70}$$

and

$$\xi = (\theta\Delta t)\frac{\partial\dot{\bar{\epsilon}}}{\partial\bar{\tau}_\theta}H_\theta. \tag{2.71}$$

Finally, the Jaumann rate of the Kirchhoff stress (Eq. (2.55)) can be obtained as,

$$\overset{\nabla}{\boldsymbol{\tau}}_\theta = \mathbf{C} : \mathbf{d}_\theta - \left(\frac{\dot{\bar{\epsilon}}_t}{1+\xi} + \frac{\xi}{(1+\xi)H_\theta}\mathbf{P}_\theta : \mathbf{d}_\theta\right)\left(\mathbf{P}_\theta + \frac{3K\alpha\chi\bar{\tau}_\theta}{\rho C_p}\mathbb{I}\otimes\mathbb{I}\right) \tag{2.72}$$

3. An efficient meshfree contact algorithm

Contact between different objects or different parts of one object is an important technical problem that exists in many engineering applications. From the perspective of computational mechanics, this is a special nonlinear problem with unknown contact boundary and reaction force. In conventional finite element method (FEM) (e.g. [4]), there are two main approaches to simulate contact and impact processes. The first approach is based on the variational method, for example the Lagrangian multiplier method, or the augmented Lagrangian multiplier method, which enforces the exact impenetrability condition; The second approach is the penalty method, even though the penalty method has been used in many commercial FEM software, it has some inherent shortcomings, such as the penalty factor is set by users subjectively, therefore the contact force may not be accurate and precise due to the arbitrariness of pre-set penalty factor. In general, the first approach is suitable for computing static or quasi-static contact, and the penalty method, the second approach, is more suitable for dynamic impact/contact problems.

Li et al. [19,20] have proposed a meshfree contact detection algorithm, it works well for meshfree simulations. In this paper, combining with the meshfree detection algorithm, we propose a coarse-to-fine meshfree contact algorithm for meshfree simulation to increase its efficiency, this method is based on the penalty method for dynamic simulations with explicit time integration, and it is adaptive for high-speed impact problem, and moreover it is very easy to be implemented.

3.1. Representation of contact systems

For a pair of interaction objects, we call the potential contact surfaces of two objects as master/slave sliding interfaces. Intuitively, the slave body is the object that initiates the contact, however, in this definition, the designation of master body and slave body can be interchanged. Initially, the contact surfaces are separate, in case of contact, there will be moment and energy transfered between two objects along the interface.

Normally, the continuous contact process can be simplified as the interaction of particles in slave sliding interface and surfaces grid in master sliding interface. Under this context, the term "particle" denotes slave particle, and the term "surface element" denotes master surface element, in 2D problems, we simply call it as master segment. Comparing with FEM, in meshfree method, a continuous object is first discretized into a set of particles, and then an interpolation field can be established based on the set of particles. Therefore, for meshfree methods, additional care is needed in order to identify master segments. For the case of self-contact, the slave nodes and master segments can locate in the same surface. For the two objects contact system, a typical contact process is illustrated in Fig. 1. Here the slave sliding interface is denoted as curve $\widehat{AB}$, and master sliding interface is curve $\widehat{CD}$.

3.2. Geometric searching

To detect contact, we first check the geometric penetration status between a slave particle and a master surface (segment). To do so, we have to find the relative position between each master segment for a given slave particle. As shown in Fig. 1, at the current configuration ($t = t_n$), the slave body is in contact with master body, but the contact position is unknown. To find contact position, we propose the following geometric searching algorithm to calculate the relative spacial position between a master/slave pair. A two-step search strategy (coarse to fine) is adopted here to accelerate computation efficiency.

3.2.1. Global searching

In the first phase, a preliminary test is carrying out between every slave particles and master particles to find the closest slave/master particles pair by spatial distance of these two particles, which is recorded in the closest particles pair array:

$$a[i] = \|r_{ij}\|_{\min}, \quad i \in 1,2,\ldots,n_s,\ j \in 1,2,\ldots,n_m \tag{3.1}$$

In above equation, i means the ith slave particle and j means the jth master particle, n_s and n_m are the total number of master and slave particles.

3.2.2. Local searching

During a dynamic contact process, if a slave particle start to penetrates a master segment, the potential master segment must contains a master particle that is closest to the slave particle, and for fixed slave particle, this master point has been identified as array $a[i]$.

However, in 2D case, a master particle connects two master segments. The corresponding slave particle can only penetrate one of them. To find out which master segment this slave particle may penetrate, we then conduct a local research. For the master segment and slave particle system shown in Fig. 2, the projection vector of the slave node to the master segment can be calculated as,

$$\lambda = \mathbf{S}\cdot\mathbf{t} \tag{3.2}$$

In above equation, $\mathbf{S} = \mathbf{rs}_j - \mathbf{rm}_m$, $\mathbf{rs}_j$ and $\mathbf{rm}_m$ denote the position of jth slave and mth master particle pair at ith time step; $\mathbf{t}$ is the tangent vector of master segment, and $\mathbf{t} = \mathbf{rm}_m - \mathbf{rm}_{m-1}$, where $\mathbf{rm}_{m-1}$ denote the master particle that connect to $\mathbf{rm}_m$.

The contact of the two bodies is possible, if

$$\boxed{0 < \lambda < 1.} \tag{3.3}$$

If contact is possible, the master segment between $\mathbf{rm}_m$ and $\mathbf{rm}_{m-1}$ will be in contact with the slave particle j, with position vector $\mathbf{rs}_j$. It is possible that the jth slave particle may penetrate this segment. It may be noted that when $\lambda = 1$, the slave particle may penetrate two master segments, and one can choose any of the two master segments to proceed further. However, in a dynamic contact process, this case rarely happens for every time steps.

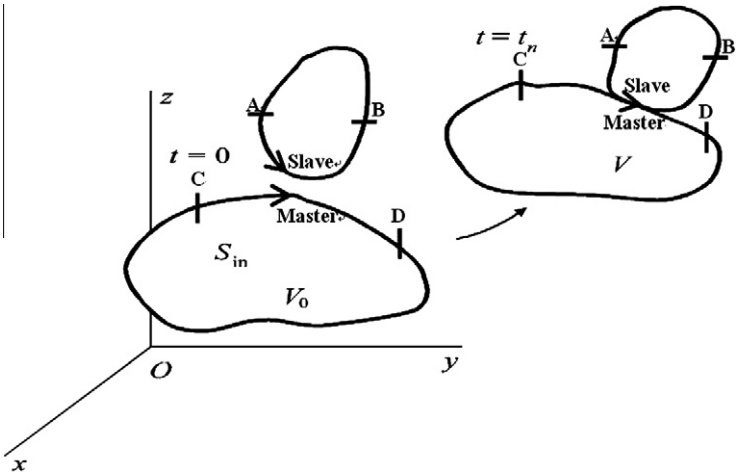

Fig. 1. Two objects contact system.

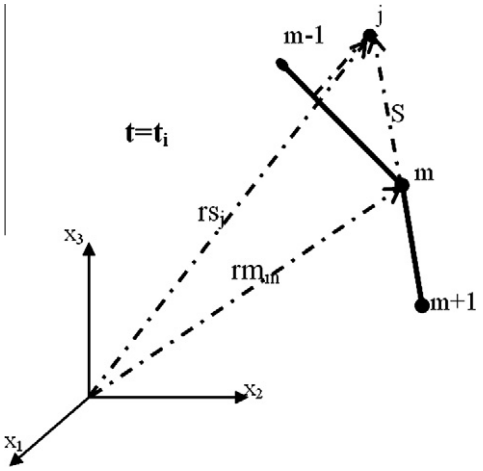

Fig. 2. Slave particle/master segment system.

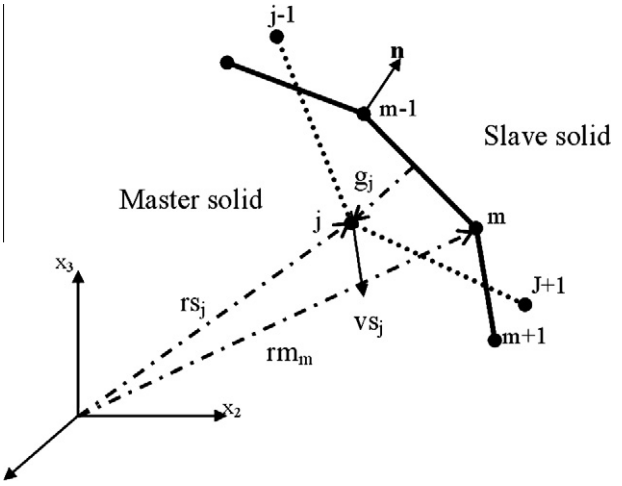

Fig. 3. The penetration condition of master/slave pair.

The above two steps searching algorithm can find and match master segment/slave particle pairs accurately. Comparing with local searching, the global searching computing is much more time consuming. However, in an explicit dynamic simulation, the deformation of configuration of solid is small during one time step, therefore, we do not need to change the initial master segment/slave particle pairs until the local searching has failed. An alternative meshfree contact algorithm is also available as described in Li et al. [19,20].

3.3. Penetration condition

Now we are at the position to address how to implement the penetration condition between the slave particle and the related master segment. To quantify the penetration characteristics, we calculate the normal gap and tangential velocity between a slave particle and master segment. Assume that the current positions of the slave particle and the related master segment are known as shown in Fig. 3. The penetration depth can be calculated as follows:

$$g_j = (\mathbf{rs}_j - \mathbf{rm}_m) \cdot \mathbf{n}_m \tag{3.4}$$

where $\mathbf{n}_i$ is the out normal of the master segment. The penetration condition can be further evaluated by checking the value of g_j:

$$g_j \begin{cases} > 0, & \text{Separation, no interaction} \\ = 0, & \text{Contaction, no interaction} \\ < 0, & \text{Penetration, interaction} \end{cases} \tag{3.5}$$

The tangential velocity that the slave particle projects to the master segment will be,

$$\mathbf{v}_j^t = \mathbf{v}_j^s \cdot \mathbf{t}_m \tag{3.6}$$

where $\mathbf{v}_j^s$ means the velocity of jth slave particle and $\mathbf{t}_i$ denotes the unit tangent tensor of master segment:

$$\mathbf{t}_m = \frac{\mathbf{rm}_m - \mathbf{rm}_{m-1}}{\|\mathbf{rm}_m - \mathbf{rm}_{m-1}\|} \tag{3.7}$$

3.4. Contact force

After contact-detection searching, the inter-penetration parts between two contact objects can be identified by the condition $g_j < 0$. The contact force can then be calculated by reinforcing the impenetrability condition. The contact force is calculated by elimination of virtual penetration. In this work, the normal and tangent contact force are obtained as the physical force that will "push back" the penetrated salve particle out of the surface master seg-

ment in one time step. If central difference time integration scheme is used, the normal contact force can be obtained as:

$$\mathbf{F}_j^n = \frac{2M_{sj}|g_j|}{\Delta t^2}\mathbf{n}_m = f_j^n \mathbf{n}_m \tag{3.8}$$

where Δt means the amount of one time step. M_{sj} is the mass of jth salve particle which penetrate through the master segment with g_j distance.

In Fig. 3, when the jth slave particle have been "push back" back to the surface of master segment, its tangent velocity will induce friction force. In this work, the classical Coulomb friction model is adopted [8] to calculate friction force.

Considering the stick condition, the friction force will be:

$$\mathbf{F}_j^{nstick} = -\frac{M_{sj}}{\Delta t}\mathbf{v}_j^t \tag{3.9}$$

Based on the Coulomb friction theory, the tangent friction force imposed by master segment to slave particle can't exceed the static friction force limit. After that, the kinetic slip friction force should be calculated by:

$$\mathbf{F}_j^{nslip} = -|\mu_k f_j^n| \frac{\mathbf{v}_j^t}{\|\mathbf{v}_j^t\|} \tag{3.10}$$

The above interaction forces are imposed to the slave particle directly. It should be noted that in meshfree simulations the force acting on an individual slave particle (primary particle) must be redistributed to all other slave particles inside the domain of influence of that slave particle, and the redistribution weight may be proportional to the inverse distance between the primary slave particle and the slave particle that the force is redistributed to.

4. Meshfree crack growth algorithm

In traditional FEM simulations, a popular approach for crack growth is the so-called element erosion technique, e.g. [13], which simply discard or "kill" the elements along the crack path. The consequence of such operation is the loss of element mass, energy, momentum, etc., which will result the loss of accuracy. Moreover, the killing element procedure cannot automatically form traction-free surface as newly-formed crack surface. From this perspective the meshfree method has its unique advantage for crack growth and crack surface representation. Belytschko et al. [7] first developed a so-called visibility condition algorithm that can provide an automatic adaptation of topological connectivity map among meshfree particles. Based on it, Li and Simonsen [22] have developed a meshfree crack growth algorithm that has been successfully used in simulations of ductile fracture.

However, in the previously published work, the cracks are pre-configured in the testing specimen, and during simulations, the cracks are kept in a state of evolution or propagation from the initial pre-notches. This setting provides an effective means to test the validity of proposed meshfree visibility condition algorithm, but in the real contact/impact process, when, where, and how the cracks grow are unknown at their initial phase. In a real fracture process, there are three phases in the whole process of crack growth: nucleation, propagation and arrest. In this work, based on the visibility condition algorithm, we propose a meshfree algorithm to simulate the all three phases of crack growth in the whole ductile fracture process automatically.

4.1. Crack nucleation

A crucial step to simulate crack nucleation and propagation in a numerical computation is how to represent the evolving crack surface and automatically adjust interpolation field around growing crack tip. This process is not only a re-interpolation scheme, but also a process of how to model the material re-configuration. For a high-speed impact induced plugging fracture problem, the cracks will nucleate at the contact surface, and go through out until they reach the opposite side of specimen. Comparing with the normal crack which has two crack tips, that means it has two potential propagation directions, shown as Fig. 4(a), the crack of plugging fracture only has one crack tip, i.e., one propagation direction, Fig. 4(b). In these pictures, each dashed circle contains one crack tip,i.e., the potential propagation direction of that crack tip. To plugging fracture, there are two one-tip-cracks, which should be nucleated at the contact surface. Using the master/slave contact algorithm described in Section 3, the cracks should always be nucleated at one of the slave particles.

The crack nucleation and growth is determined by a specified criterion, such as the damage criterion or the strain intensity factor criterion. For example, if the accumulating damage value D is chosen as the index of crack nucleation and growth criterion, which is based on a specified model, such as the Johnson–Cook model. To nucleate a new crack tip, in each time step, we apply the criterion D_c to every salve particles that is defined by the contact/impact algorithm. Once the damage value D_i which is attached to one of those particles, P_i, exceeds the crack growth criterion D_c, particle P_i will be identified as a crack core. To form a one-tip-crack shown in Fig. 4(b), we need to find the next particle P_j whose damage value is bigger than D_c, and it locates around the crack core inside a circle with radius R centered at P_i in the following time steps. After two damaged particles are selected, the second damaged particle will become the crack tip, and the crack core particle P_i will be split to two new particles that have the same value of state variables at the moment of splitting, shown in Fig. 5, here the salve particles are marked as diamond black boxes, the particles locate at the surface of crack (except crack tip) are marked as square black boxes, the normal meshfree particles are marked as circle black dotes and the virtual points which denote the crack path are marked as diamond blank boxes. In Fig. 5, particle P_i becomes a virtual point P_1 between the newly split two particles. Particle P_j is the crack tip attached to a specified meshfree particle, the segment line $\overline{P_1P_j}$ denotes the path of crack.

The mass and volume of the two new particles are re-assigned according to the following particle splitting method:

$$Mass_{new1} = \frac{1}{2}Mass_{old} \tag{4.1}$$

$$Mass_{new2} = \frac{1}{2}Mass_{old} \tag{4.2}$$

and

$$Volume_{new1} = \frac{1}{2}Volume_{old} \tag{4.3}$$

$$Volume_{new2} = \frac{1}{2}Volume_{old} \tag{4.4}$$

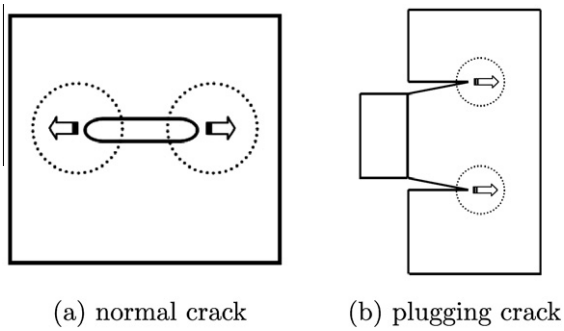

Fig. 4. The geometric morphologies of cracks.

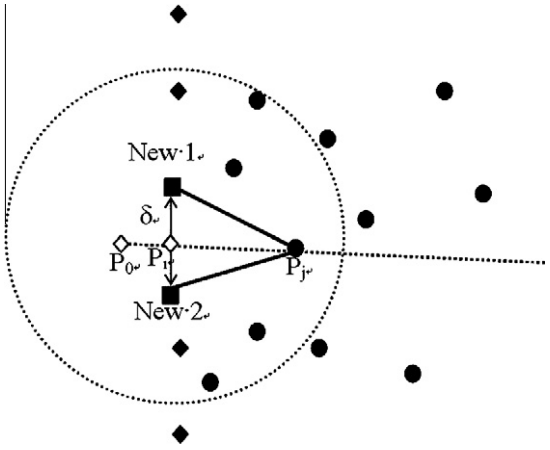

Fig. 5. Illustration of numerical scheme for crack nucleation.

The kinematic field variables, such as displacement, velocity, and acceleration of the new particles are assigned based the following formulas:

$$\mathbf{X}_{new1} = \mathbf{X}_i + \boldsymbol{\delta}, \tag{4.5}$$

$$\mathbf{X}_{new2} = \mathbf{X}_i + \boldsymbol{\delta}; \tag{4.6}$$

$$\mathbf{Disp}_{new1} = \mathbf{Disp}_{old} + \boldsymbol{\delta} \tag{4.7}$$

$$\mathbf{Disp}_{new2} = \mathbf{Disp}_{old} - \boldsymbol{\delta} \tag{4.8}$$

$$\mathbf{Vel}_{new1} = \mathbf{Vel}_{old} \tag{4.9}$$

$$\mathbf{Vel}_{new2} = \mathbf{Vel}_{old} \tag{4.10}$$

$$\mathbf{Acc}_{new1} = 0.0d0 \tag{4.11}$$

$$\mathbf{Acc}_{new2} = 0.0d0 \tag{4.12}$$

where $\boldsymbol{\delta}$ is vector who is vertical with the crack path segment $\overline{P_1P_j}$ and whose length $|\boldsymbol{\delta}| \ll 1$. It serves the purpose to make a physical distinction of the two new particles once they are separated.

After the spatial shape of a one-tip-crack is formed, shown as in Fig. 5, two new surface segments will be generated in the fracturing body, which will change the topological or configurational structure of the solid. To correctly reflect such change, the meshfree interpolation field has to change accordingly. One has to develop a numerical algorithm that can automatically modify the local connectivity map for meshfree particles, so that the computation can simulate a running crack without the user interference. To do so, we adopt the parametric visibility condition algorithm proposed by Li and Simonsen [22] to update the connectivity arrays of the related particles and hence the shape of meshfree interpolation function for particles nearby the point P_1. To implement the visible condition, the segment line $\overline{P_0P_j}$ is used to 'cut' the straight line connecting the nearby particles with P_1, where the virtual particle P_0 is defined as:

$$P_0 = P_1 + \delta \frac{\vec{P_1P_j}}{|\vec{P_1P_j}|} \tag{4.13}$$

where δ is a scalar and $\delta \ll 1$, which means that we only extend the segment line $\vec{P_1P_j}$ a δ ratio to 'cut' the particle connection clearly.

4.2. Crack propagation

Once the projectile impact specimen, the nucleated cracks begin to propagate deeply inside solid. Assume that there is a crack with crack tip particle P_n and the piece-wise segment crack path line $\overline{P_0P_1 \cdots P_n}$, shown as Fig. 6. In this work, during the crack propagation process, a crack tip is always attached to an existing material/interpolation particle. It only moves from one particle to another. The crack growth is determined by the particle damage value D too. To locate the new crack tip, we first choose a radius R and draw a circle centered at the current crack tip P_n, then apply the crack criterion D_c to each meshfree particle inside the circle to decide which point should be the next crack tip, except those points (square boxes) on the crack surfaces.

In practice, however, if the new crack tip is located behind the current crack tip, it could cause some complications such as the crack-direction-reverse phenomenon. To simplify the crack growth algorithm, we limit the potential new crack tip inside a fan region of the circle, which is defined by the angle $\angle AOB$ in Fig. 6. That angle is centered at the segment line of $\overline{P_{n-1}P_n}$ with a half of angle θ_c, here, $\overline{P_{n-1}P_n}$ is the last crack path segment.

For a specified particle P_j inside the circle, the angle between segment line $\overline{P_nP_j}$ and $\overline{P_{n-1}P_n}$ can be represented as:

$$\theta_j = \arccos\left(\frac{\vec{P_{n-1}P_n} \cdot \vec{P_nP_j}}{|\vec{P_{n-1}P_n}||\vec{P_nP_j}|}\right) \tag{4.14}$$

Finally, the new crack tip can be selected by satisfying the following criteria:

$$D_j \geqslant D_c \quad \text{and} \quad \theta_j \leqslant \theta_c/2.0 \tag{4.15}$$

When there are more than one particle whose damage value exceeds the critical damage value, it will cause another technical complexity: crack bifurcation. For simplicity, in this work we only consider one particle as the new crack tip, i.e., the particle with maximum damage value.

Once the new crack tip is selected, we split the old crack tip into two particles using a similar algorithm as that in Eq. (4.4). However, at the crack propagation phase, the mass and volume of the new two particles are re-assigned based on the angle defined by the crack propagation direction. Denote the angle $\angle P_jP_nP_1$ as φ_1 and angle $\angle P_1P_nP_j$ as φ_2, which satisfy the condition $\varphi_1 + \varphi_2 = 2\pi$ as shown in Fig. 6. Then the particle split algorithm is

$$Mass_{new1} = \frac{\varphi_1}{2\pi} Mass_{old} \tag{4.16}$$

$$Mass_{new2} = \frac{\varphi_2}{2\pi} Mass_{old} \tag{4.17}$$

and

$$Volume_{new1} = \frac{\varphi_1}{2\pi} Volume_{old} \tag{4.18}$$

$$Volume_{new2} = \frac{\varphi_2}{2\pi} Volume_{old} \tag{4.19}$$

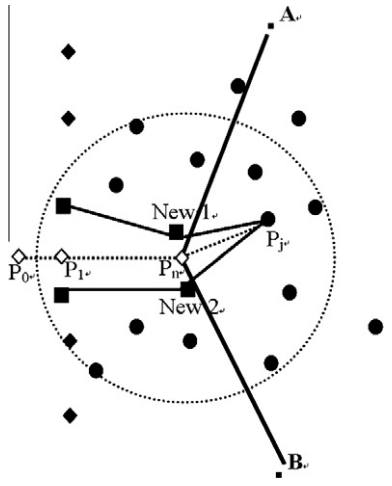

Fig. 6. Illustration of numerical scheme for crack growth.

The kinematic field variables, such as displacement, velocity, and acceleration of the new particles are assigned as the algorithm exactly described in Eqs. (4.5)–(4.12).

Once the crack propagation finish, the current crack tip become particle P_j. When a crack propagates one step forward, the crack surface segments inside solid will be update too. In the fracturing body, the visible condition algorithm is adopted to modify the particle integration connection again. At the current crack propagation step, the segment line $\overline{P_nP_j}$ is used to 'cut' the integration connection of particles that located nearby the current crack tip.

For the ductile fracture, the shape of crack surface is complex. In following, an example is illustrated to display the meshfree shape function evolution of a particle that is located along a crack path. Before the crack reaches to that particle, its original shape function is a single "hill" as shown in Fig. 7(a) and (b) after the crack passes through it, the particle is split into two particles to form new crack surfaces via particle splitting algorithm. Sequentially the local topological structure of the solid has changes, hence we update the meshfree connectivity by the parametric visibility condition. In Fig. 7 (c) and (d), the modified 2D and 3D profiles of shape function distribution show that a meshfree function has been cut by crack into two parts, and each part is assigned to one of the split particle. The example shows alone crack path, the meshfree shape function can be automatically updated successfully.

4.3. Crack arrest

In the plugging fracture, once a crack goes through the specimen, the crack will severe the specimen, and the crack will stop to propagate, which we call as the crack arrest. To simulate crack arrest phenomenon, we have developed the following meshfree algorithm. At each crack propagation step, once the new crack tip is found, it should be tested whether it is located in the outer surface of specimen or not. Because meshfree is a meshless simulation, a specified strategy must be designed to test the outer surface condition. In this paper, we use the angle θ_j, which is described in Eq. (4.14) to estimate the outer surface condition. In Fig. 6, for every particle inside the searching circle, we must calculate the angle θ_j to find out the new crack tip. If no new crack tip can be found out at the current step, and the maximum an minimum angle θ_{max} and θ_{in} satisfy the following condition:

$$\theta_{max} - \theta_{in} > \theta_c \tag{4.20}$$

we then say that the current crack tip P_n locates at the outer surface of specimen, and the crack should be arrested.

For an arrested crack tip, we have first implemented the particle split method mentioned in Eqs. (4.4) and (4.12) to split particle P_n to two new particles. Subsequently the crack path segment $\overline{P_{n-1}P_{n+1}}$ is used to modify the integration field of particles based on visible condition algorithm, shown in Fig. 8. Here the virtual point P_{n+1} is defined by:

$$P_{n+1} = P_n + \delta \frac{\vec{P_{n-1}P_n}}{|\vec{P_{n-1}P_n}|} \tag{4.21}$$

where δ is a scalar and $\delta \ll 1$. The same as crack nucleation, we only extend the segment line $P_{n-1}P_n$ a δ ratio to 'cut' the particle connection clearly.

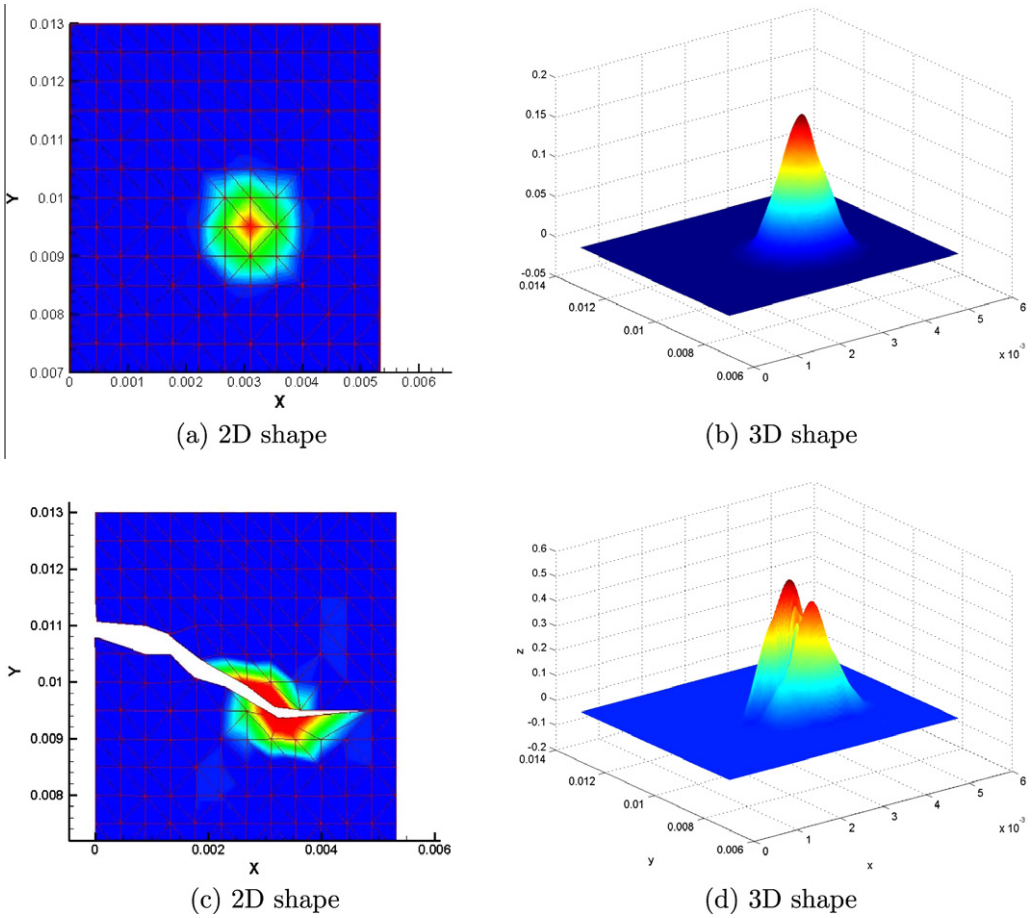

Fig. 7. Meshfree shape function evolution along crack propagation.

5. Numerical simulations

5.1. Crack growth criteria

The most critical step in simulation of plugging fracture is the crack growth criterion, which determines whether or not the numerical simulation makes any physical sense. The main mechanism of plugging fracture is attributed to the formation of adiabatic shear banding (ASB) and subsequent damage accumulation inside the ASB, e.g. [31]. Therefore, in this work, we have proposed two fracture criteria in numerical simulations. Firstly, we choose the effective shear strain as the fracture criterion, i.e. we set up a critical effective shear strain value, ϵ_{cr}. Once the effective shear strain value is reached at one point near a crack tip, the crack starts to advance.

Secondly, we choose the accumulative damage value as the crack growth criterion. In the meshfree formulation, the Johnson–Cook damage model [28] is adopted to estimate the damage of particles, which is calculated by the following damage evolution equation:

$$D = \sum \frac{\Delta\epsilon}{\epsilon_f} \tag{5.1}$$

where

$$\epsilon_f = \left[D_1 + D_2 \exp\left(D_3 \frac{\tau_m}{\sigma_Y}\right)\right][1 + D_4 \ln \dot{\epsilon}][1 + D_5 T] \tag{5.2}$$

and $\tau_m = \frac{1}{3}(\tau_{11} + \tau_{22} + \tau_{33})$, $\Delta\epsilon$ is the plastic strain increment in each time step, and D_1, D_2, D_3, D_4, D_5 are material damage constants. Once a critical damage value D_{cr} is reached at a particles around a crack tip, the crack front will advance to a new position

5.2. Numerical modeling

To validate the meshfree algorithm of the thermo-mechanical formulation, we have performed numerical simulations of a plugging fracture failure experiment conducted by Borvik et al. [10]. The experimental set-up is shown in Fig. 9. To validate the numerical result with experimental data, two cases of simulations are carried out according to the exact experiment conditions that are documented in Table 1. In the Case I and the Case II, the width of target plate is 11.1 mm and 10.2 mm, respectively, corresponding to the experiment Test 8-13 and Test 8 from Borvik et al. [10]. In Borvik et al.'s experiment, the projectile is launched by compressed gas gun with variable velocity to impact a thin target plate. After contacting, the high speed stress wave induces growth of micro-cracks and micro-voids inside shear zone with heat generation and conduction from plastic work. Subsequently, discontinuous micro-cracks will coalesce each other to form the macro-crack, and that crack propagate to grow through the target to form the plugging failure. The final damage pattern can be shown as Fig. 10. In experiments, the projectile is made of hardened steel, and the target is made of Weldox 460E steel. Comparing with target plate, the final deformation of projectile is very small (see Figs. 13 and 14). Therefore in this work, we model the projectile as a rigid body, and we model the target plate by using the Johnson–Cook model with constants tabulated in Table 2. The material constants of the Johnson–Cook model are taken from the experimental data in Borvik et al. [10] exactly. In Borvik et al. [10], a set of systematic experiments have been conducted to measure Welddox 460E steel and to determine the material constants of the Johnson–Cook model. In this work, the fracture criteria is chosen based on either the critical shear strain or the critical damage. The critical value for the shear strain is set as $\epsilon_{cr} = 0.30$, and the critical damage value is set as $D_{cr} = 0.50$ for the Johnson–Cook damage model.

In meshfree discretization, on the vertical direction,we use non-uniform graded particle distribution, i.e., we use a dense particle distribution near the impact area, and gradually coarsen the particle density towards to the ends of plate. While on the plate thickness direction, we set uniform graded particle distribution over the plate thickness. To test the convergence of proposed method, two meshfree particle distributions are used in the simulation: a coarse particle distribution/discretization that contains 11,520 particles for meshfree interpolation and 44,068 quadrature points for numerical integration; and a fine particle distribution/discretization that contains 45,984 particles and 179,916 quadrature points. Our simulation computer is Hp xw4600 workstation (CPU: Intel Core 2 Duo 2.83 GHZ, RAM:3.0 GB). For Case I with effective shear

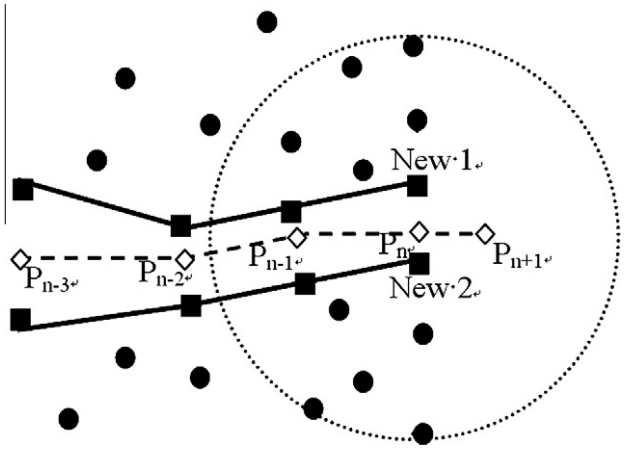

Fig. 8. Illustration of numerical scheme for crack arrest.

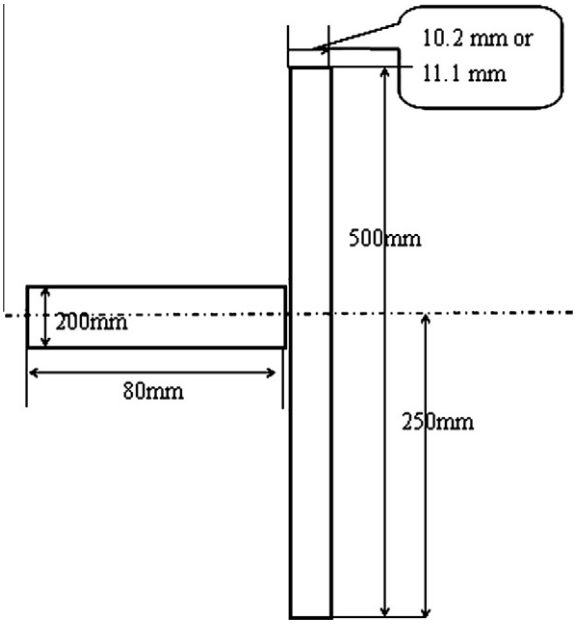

Fig. 9. The dimension of computation configure.

Table 1
Simulation conditions.

Test ♯	Target width (mm)	Projectile initial velocity (m s^{-1})
Case I	11.1	298.0
Case II	10.2	173.7

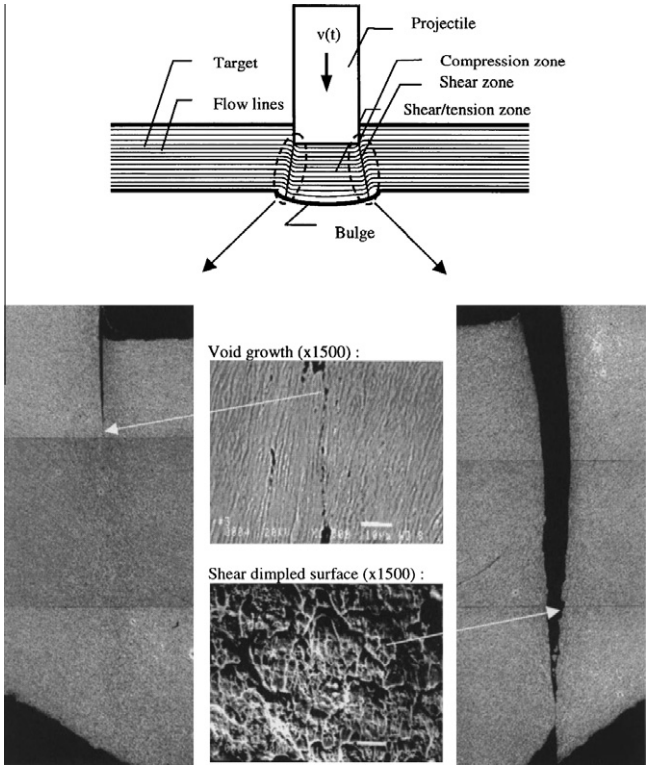

Fig. 10. The damage pattern of plugging failure. (From Borvik et al. [9] with the permission of Elsevier Pub. Co.).

Table 2
Material parameters of Weldox 460E steel.

Parameter	Value	Definition
E	200 GPa	Young's modulus
v	0.3	Poisson's ratio
ρ	7850 kg m^{-3}	mass density
A	490 MPa	yield stress
B	807 MPa	strain hardening
n	0.73	strain hardening index
$\dot{\epsilon}_0$	1.0 s^{-1}	reference strain rate
m	0.94	temperature softening
C_p	452 J (kg K)$^{-1}$	specific heat
α	11.2 $\times$ 10^{-6} K^{-1}	coefficient of thermal expansion
χ	0.9	the fraction of plastic work converted to heat
k	452 J (kg K)$^{-1}$	specific heat
D_1	0.0705	damage parameter
D_2	1.732	damage parameter
D_3	−0.54	damage parameter
D_4	−0.015	damage parameter
D_5	0	damage parameter

strain criteria, the computing response time is 118.0 μs, the computing time for coarse discretization is 0.92 h and for fine discretization is: 3.80 h. For Case II with effective shear strain criteria, the computing response time is 216.0 μs, computing time for the case of coarse discretization is 1.86 h, and for the case of the fine discretization is it is 7.1 h. The CPU time for Johnson–Cook damage criteria is very close to the above data.

5.3. Simulation details

The residual velocity of projectile v_p after plugging failure is a main measurable quantity or characteristics of the ballistic penetration test. Results of numerical simulation and experiment of both Case I and Case II are compared in Figs. 11 and 12. The comparison data is shown as Table 3, where v_i denotes the projectile initial velocity, v_p^e denotes the residual velocity of projectile from experiment, and v_p^s denotes the residual velocity of projectile from numerical simulation.

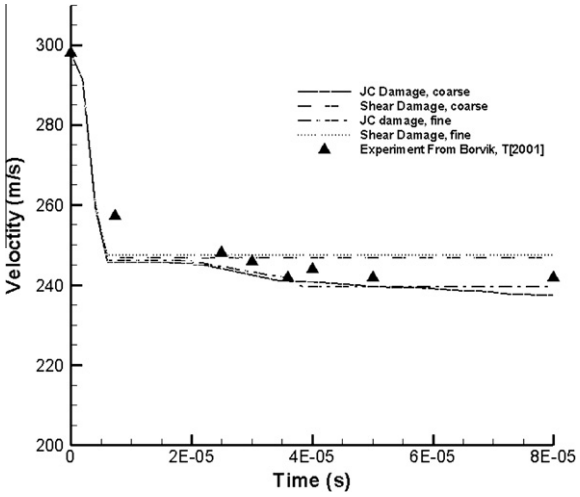

Fig. 11. Comparison on the residual velocities of projectile between experiment and simulation: Case I.

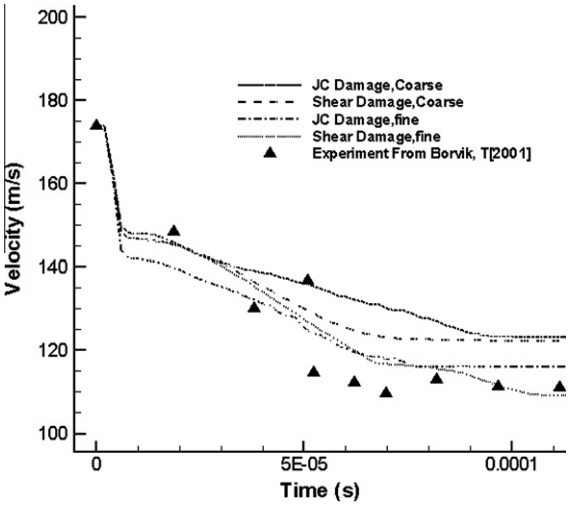

Fig. 12. Comparison on the residual velocities of projectile, between experiment and simulation: Case II.

Summing up the comparison, we find that for Case I both of the coarse and fine discretization are convergence to the experiment data well, whereas for Case II, the error of simulation decreases

Table 3
Residual velocity of projectile.

Test ♯	Particles	v_i	v_p^e (m s^{-1})	Criteria	v_p^s (m s^{-1})	Error (%)
Case I	11,496	298.0	241.4	Damage	238.5	−1.2
				Effective strain	246.7	+2.2
	45,984			Damage	239.6	−0.8
				Effective strain	246.1	+1.9
Case II	11,496	173.7	112.0	Damage	123.0	+9.8
				Effective strain	121.8	+8.7
	45,984			Damage	116.1	3.6
				Effective strain	109.4	−2.6

from about 9% to 3%. Even though the specimen of Case II is a little thinner than Case I (10.2 mm vs. 11.1 mm), because the projectile velocity of Case II is lower than Case I (173.7 m s^{-1} vs. 298.0 m s^{-1}), the plastic deformation time of Case II is longer than that of Case I (see Figs. 13 and 14). From Fig. 10, we can find that the plugging fracture is a localization phenomena, therefore, the simulation results show that the simulation of plugging fracture is discretization dependent.

Although the simulation results show that both the damage and the effective shear strain criteria work well, as pointed out by Bai et al. [3], the damage mechanism of high-speed impact is associated with the mode II fracture, and strain localization will cause void growth and heat generation inside the shear bands. Hence, in the following, we mainly discuss the numerical results based on the effective strain criterion for the case of the fine discretization.

In Borvik et al. [10], there are some high-speed camera images for both Case I and Case II at specific time instances. To compare the deformation morphology of these tests, the experimental and numerical results are juxtaposed in Figs. 13 and 14. The variations of the color in the figures are the contours of effective stress, where the 'red[1]' area indicates a more than 1.2×10^9 Pa high stress zone. From the figure, we can observe the penetration of the projectile and the whole process of the plugging fracture. For the Case I, the plugging fracture process is finished at 28 μs after the initial impact, i.e., the crack goes through the specimen. And it occurs at 46 μs for the Case II as shown in Figs. 13 and 14.

The distribution of the effective stress is also displayed in these figures. One may observe that a high stress zone moves with the crack tip along the crack path, and the stress wave propagation inside the target plate may also be observed. Owing to the fact that the plugging failure of metal is an extraordinary nonlinear material response, the dynamical crack growth process in the target renders a non-symmetric fracture pattern. In Figs. 13 and 14, one may find that the fracture surfaces of cracks have rough and irregular shapes, which indicates a ductile fracture feature. Paying attention to the shape of the final shape of the plugging crack, one can find a distinct plastic deformation pattern at the left of top and bottom side of plugging crack, that is a clear evidence of ductile fracture, and it is difficult to be simulated by FEM methods because of mesh constraints.

The detailed failure morphology of Case I is plotted as the contour of shear stress in Fig. 15. When the projectile impacts the target, the high-speed dynamic indentation causes massive plastic deformation at the contact region of the target. Subsequently the damage of particles located nearby edges of the projectile quickly increases to reach the critical value, then the cracks start to propagate through the target.

From Fig. 15, we can find that during crack propagation the shear stress is localized in a small and almost horizontal zone from the vertical edge of target. Outside the localized deformation zone, the high shear stress disappears rapidly. Back to the localized deformation zone, we can find that the high shear stress zone concentrates at the front of crack tips (the "red" and "blue" areas) and it gradually lessens after the cracks have severed target plate. This phenomena indicates that the stress has been released by the newly-formed crack surface, and it indirectly validates the fact that the trace-free crack surface has been modeled correctly in the meshfree simulation. Such fracture feature is difficult to be captured by the FEM erosion algorithm.

Reviewing the morphology of the crack surface, one may see a zig-zag pattern. This zig-zag pattern of rough crack surface is the trademark of ductile fracture [32–34]. Using the grid based simulation method such as FEM, the path of crack growth should go along the edges of elements, then it is hard to capture this rough

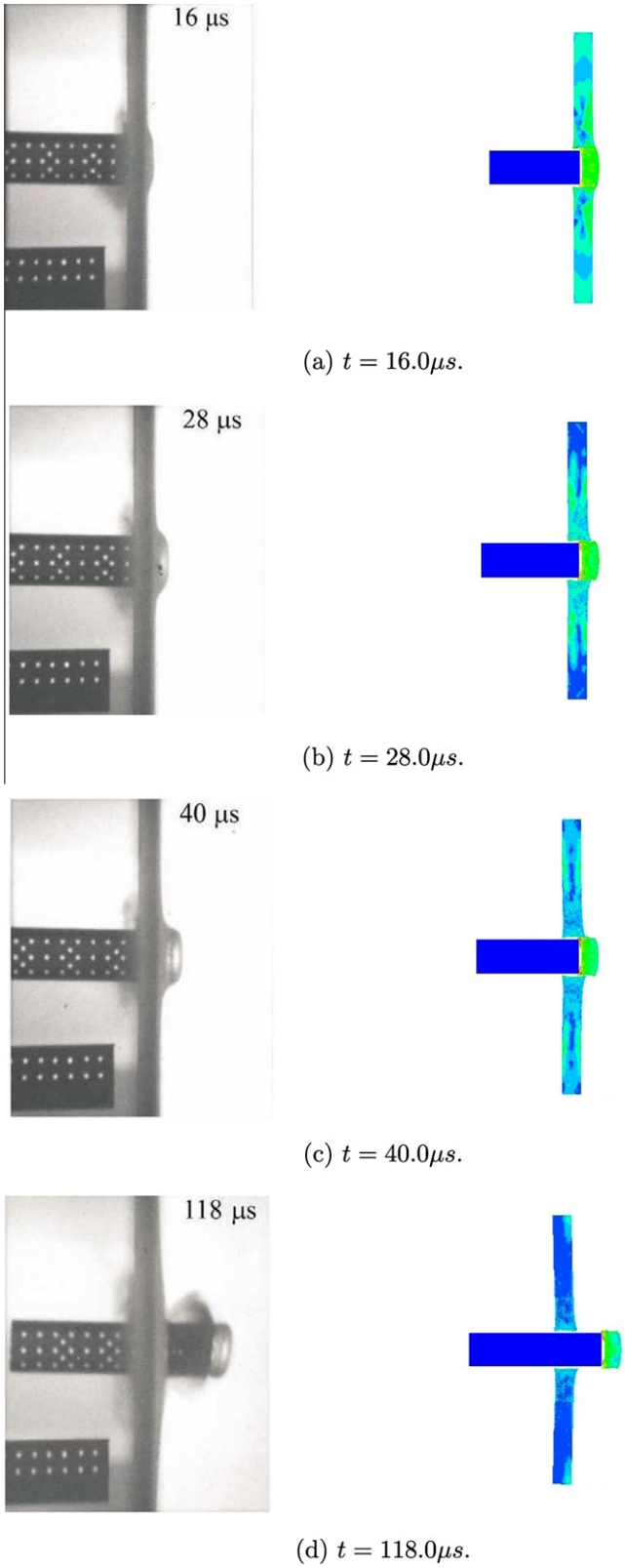

Fig. 13. High speed camera images compare with numerical simulation: Case I, v_i = 298.0 m s^{-1}. The numerical plots is shown as contours of the effective stress σ_{eq}. (From Borvik et al. [9] with the permission of Elsevier Pub. Co.).

[1] For interpretation of colour in Figs. 7, 13, 14, 16 and 17, the reader is referred to the web version of this article.

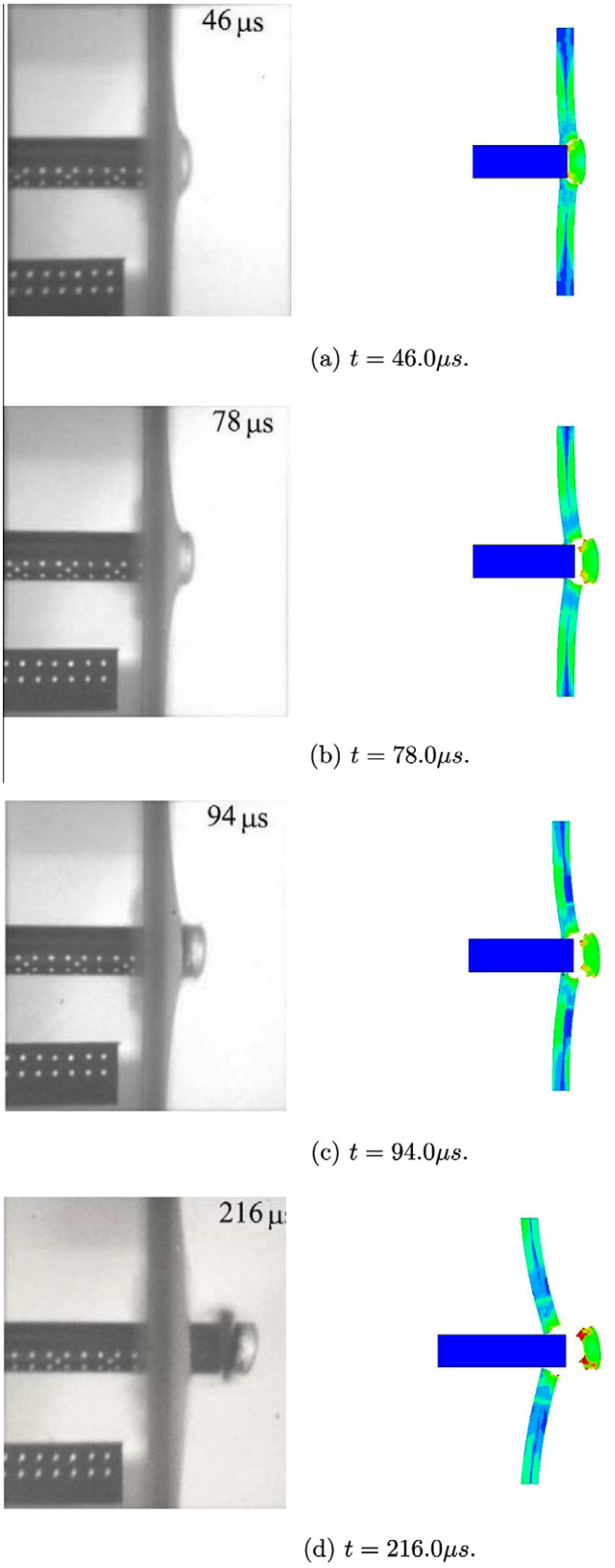

(a) $t = 46.0\mu s$.

(b) $t = 78.0\mu s$.

(c) $t = 94.0\mu s$.

(d) $t = 216.0\mu s$.

Fig. 14. High speed camera images compare with numerical simulation: Test Case II, $v_i = 173.7$ m s^{-1}. The numerical plots is shown as contours of effective stress σ_{eq}. (From Borvik et al. [9] with the permission of Elsevier Pub. Co.).

surface feature of ductile fracture. The final fracture morphologies of Case I with coarse and fine discretization at 34 μs are shown as Fig. 16. In these figures, we can find that the crack surface morphology maintains its rough feature and it becomes finer for the computation result obtained from the fine particle discretization.

We have studied the numerical instability of the meshfree simulations by changing different time increment in time integration.

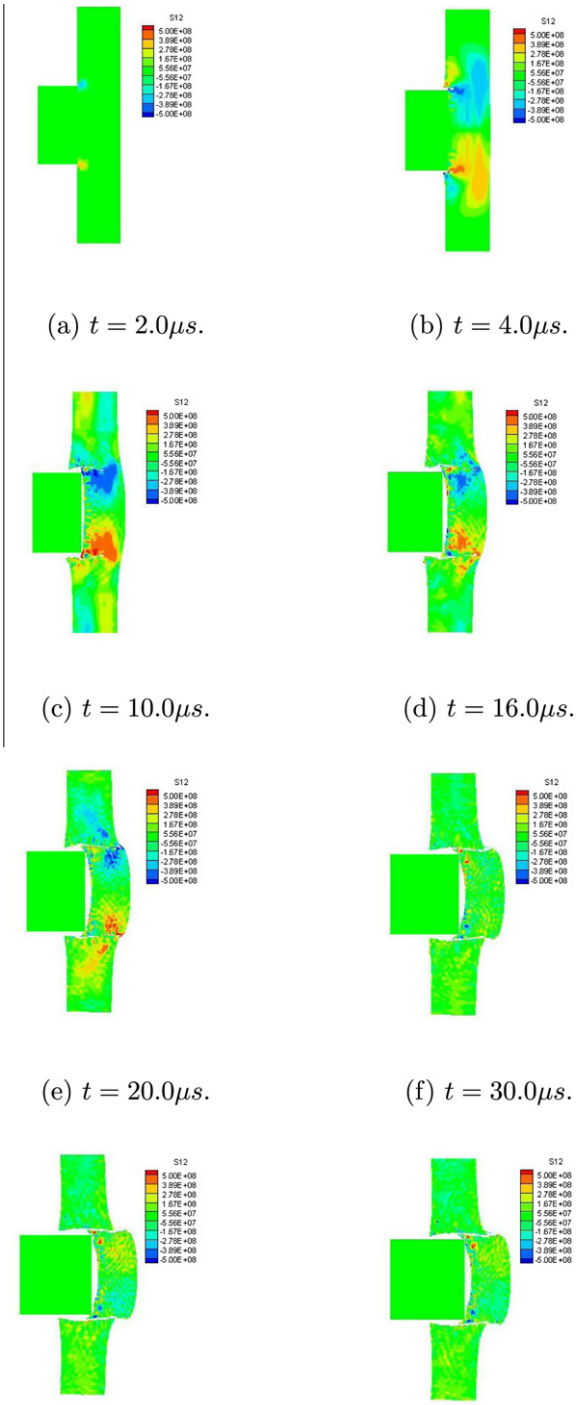

(a) $t = 2.0\mu s$.

(b) $t = 4.0\mu s$.

(c) $t = 10.0\mu s$.

(d) $t = 16.0\mu s$.

(e) $t = 20.0\mu s$.

(f) $t = 30.0\mu s$.

(g) $t = 34.0\mu s$.

(h) $t = 36.0\mu s$.

Fig. 15. The detailed crack surface morphology with a background of shear stress contour σ_{12}.

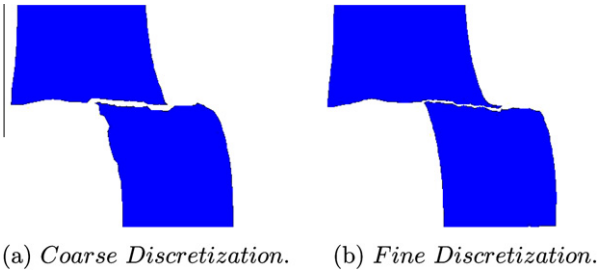

Fig. 16. The crack surface morphology of coarse and fine discretization.

For the simulation results reported above, we have used a very small time increment, $\Delta t = 4 \times 10^{-9}$ s, in the simulations for both coarse particle distribution and the fine particle distribution. It is well below the Courant–Friedrichs–Lewy (CFL) instability limit for linear problems. On the other hand, we have also tested other time increments starting from $\Delta t = 10^{-9}$ s to 10^{-7} s. For the fine particle distribution, the numerical instability occurs between $\Delta t = 5.0 \times 10^{-7}$ s to 10^{-8} s. It is worthy mentioning that the CPU time of the computation reported above is also related to time increment used in time integration. From this perspective, the reported CPU time is a conservative estimate.

Zooming into the contact interface, one may find that initially the projectile impacts on the target with its whole front end; subsequently with the projectile penetration progressing, there is an air gap formed between the front end of the projectile and the contact surface of the target, which may be due to the "bending effect" of the target plate caused by the impact load. This makes the contact force concentrating in a small zone nearby the two plugging cracks.

During the plastic deformation, the plastic work converts to heat that further induces thermal softening. For the Case I, the local temperature profiles of target are shown in Fig. 17. When temperature reaches a critical value inside the adiabatic shear band, the crystal grains will undergo recrystallization, which will further lead to the stress collapse inside the ASB, and it will result adiabatic shear band propagation. From Fig. 17, one can observe that the temperature is localized near the damage zone, and it is related to strain localization; these simulation results agree with the early results of meshfree simulations of adiabatic shear bands reported by Li et al. [19–21].

6. Discussions

In this work, we have developed a meshfree procedure to simulate ductile plugging fracture problem under real contact/impact condition. Comparing with experiment data, the numerical computation shows that proposed algorithm can accurately simulate the ductile fracture undergoing finite deformations and large scale yielding.

The meshfree formulation presented here has some special features, including (1) A coupled thermal–mechanical formulations for meshfree computation; (2) A modified rate-dependent constitutive update algorithm for finite deformations; (3) An effective meshfree impact/contact algorithm for dynamics simulation; (4) A meshfree crack growth and propagation algorithm that can automatically simulate the crack nucleation, propagation and arrest. Moreover, the numerical computation presented here illustrates that proposed formulas are effective and computationally stable; the proposed meshfree contact/impact algorithm is simple and efficient comparing with the previous meshfree version, and it can be easily extended to 3D simulations.

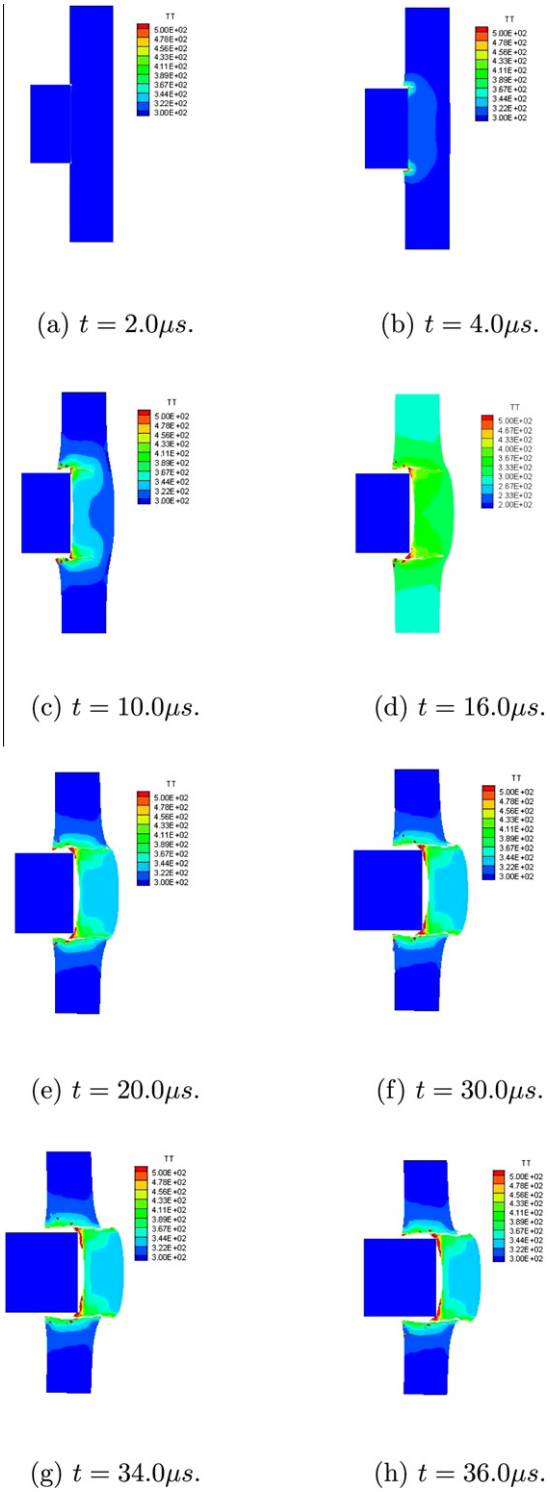

Fig. 17. The detailed crack surface morphology with a background of temperature profile.

Finally, like most of other numerical simulations, we cannot completely eliminate mesh sensitivity, especially for the fracture problem, where the stress and temperature fields are extraordinarily localized at the crack tip zone, which make mechanical variables such as the damage value dependent on particle distribution. Nevertheless, we believe that the simulation presented here has captured the main features of ductile plugging fracture and the related dynamical mechanical responses.

Acknowledgments

This work is supported by a grant from Army Research Laboratory to NextGen Aerospace Co., which sub-contracted to the University of California at Berkeley. Dr. T.W. Wright of Army Research Laboratory is the technical advisor.

References

[1] Ambrósio JAC. Contact and impact models for vehicle crachworthiness simulation. Int J Crachworthiness 2003;8:73–86.
[2] Armero F, Simo JC. A priori stability estimate and unconditionally stable product formula algorithm for nonlinear coupled thermoplasticity. Int J Plasticity 1993;9:749–82.
[3] Bai Y, Dodd B. Adiabatic shear band localisation. New York: Pergamon Press; 1992.
[4] Bathe KJ. Finite element procesures. London: Prentice-Hall; 1996.
[5] Belytschko T. On computational methods for crashworthiness. Comput Struct 1992;42:271–9.
[6] Belytschko T, Lu YY, Gu L. Element-free Galerkin methods for static and dynamic fracture. Int J Solids Struct 1995;32:2547–70.
[7] Belytschko T, Lu YY, Gu L. Crack propagation by element-free Galerkin methods. Eng Fract Mech 1995;51:295–315.
[8] Belytschko T, Liu WK, Moran B. Nonlinear finite elements for continua and structures. Chichester: Wiley; 2000.
[9] Borvik T, Langseth M, Hopperstad OS, Malo KA. Ballistic penetration of steel plates. Int J Impact Eng 1999;22:855–86.
[10] Borvik T, Hopperstad OS, Berstad T, Langseth M. Numerical simulation of plugging failure in ballistic penetration. Int J Solids Struct 2001;38:6241–64.
[11] Borvik T, Hopperstad OS. Effect of target thickness in blunt projectile penetration of Weldox 460 E steel plates. Int J Impact Eng 2003;28:413–64.
[12] Camacho GT, Ortiz M. Adaptive Lagrangian modelling of ballistic penetration of metallic targets. Comput Methods Appl Mech Eng 1997;142:269–301.
[13] Chen EP. Numerical simulation of shear induced plugging in HY100 steel plates. Int J Damage Mech 1992;1:132–43.
[14] Fleming M, Chu YA, Moran B, Belytschko T. Enriched element-free Galerkin methods for crack tip fields. Int J Numer Methods Eng 1997;40:1483–504.
[15] Johnson GR, Cook WH. A constitutive model and data for metals subjected to large strains, high strain rates and high temperature. In: Proceedings of the 7th international symposium on ballistics; 1983. p. 1–7.
[16] Johnson GR, Cook WH. Fracture characteristics of three metals subjected to various strains, strain rates, temperatures and pressures. Eng Fract 1985;21:31–48.
[17] Kang WJ, Cho SS, Huh H, Chung DT. Modified Johnson–Cook model for vehicle body crashworthiness simulation. Int J Vehicle Design 1999;21:424–35.
[18] Li S, Liu WK. Numerical simulations of strain localization in inelastic solids using meshfree methods. Int J Numer Methods Eng 2000;48:1285–309.
[19] Li S, Liu WK, Qian D, Guduru P, Rosakis AJ. Dynamic shear band propagation and micro-structure of adiabatic shear band. Comput Methods Appl Mech Eng 2001;191:73–92.
[20] Li S, Qian D, Liu WK, Belytschko T. A meshfree contact-detection algorithm. Comput Methods Appl Mech Eng 2001;190:3271–92.
[21] Li S, Liu WK, Rosakis AJ, Belytschko T, Hao W. Meshfree Galerkin simulations of dynamic shear band propagation and failure mode transition. Int J Solids Struct 2002;39:1213–40.
[22] Li S, Simonsen BC. Meshfree simulations of ductile crack propagation. Int J Comput Methods Eng Sci Mech 2004;6:1–19.
[23] Li S, Liu WK. Meshfree particle method. Berlin, Germany: Springer-Verlag; 2004.
[24] Lin TZ, Yang Q, Tan C, Liu B, McDonald A. Processing and ballistic performance of lightweight armors based on ultra-fine-grain aluminum composites. J Mater Sci 2008;43:7344–8.
[25] Peirce D, Shih CF, Needleman A. A tangent modulus method for the rate dependent solids. Comput Struct 1984;18:168C173.
[26] Rabczuk T, Song J-H, Belytschko T. Simulations of instability in dynamic fracture by cracking particles methods. Eng Fract Mech 2009;76:730–41.
[27] Simonsen BC, Li S. Meshfree modeling of ductile fracture. Int J Numer Methods Eng 2004;60:1425–50.
[28] Simkins DC, Li S. Meshfree simulations of ductile failure under thermal-mechanical loads. Comput Mech 2006;38:235–49.
[29] Taylor G, Quinney H. The latent energy remaining in a metal; after cold working. Proc Roy Soc 1934;143:307–26.
[30] Wawrzynek PA, Ingraffea AR. Interactive finite element analysis of fracture processes: an integrated approach. Theor Appl Fract Mech 1987;8:137–50.
[31] Wright WT. The physics and mathematics of adiabatic shear bands. Cambridge, UK: Cambridge University Press; 2002.
[32] Xia L, Shih CF, Hutchinson JW. Computational approach to ductile crack growth under large scale yielding conditions. J Mech Phys Solids 1995;43:389–413.
[33] Xia L, Shih CF. Ductile crack growth – II. Void nucleation and geometry effects on macroscopic fracture behavior. J Mech Phys Solids 1995;43:1953–81.
[34] Xia L, Shih CF, Hutchinson JW. A computational approach to ductile crack growth under large scale yielding conditions. J Mech Phys Solids 1995;43:389–413.
[35] Yadav S, Repetto EA, Ravichandran G, Ortiz M. A computational study of the influence of thermal sofening on ballistic penetration in metals. Int J Impact Eng 2001;25:787–803.
[36] Zhou M, Rosakis AJ, Ravichandran G. Dynamically propagating shear bands in impact-loaded prenotched plates – I. Experimental investigations of temperature signatures and propagation speed. J Mech Phys Solids 1996;44:981–1006.
[37] Zhou M, Ravichandran G, Rosakis AJ. Dynamically propagating shear bands in impact-loaded prenotched plates – II. Numerical simulations. J Mech Phys Solids 1996;44:1007–32.